Deep Volume Reconstruction from Multi-focus Microscopic Images

Caio Azevedo[1], Sanchayan Santra[2][0000−0002−5770−8611], Sudhakar Kumawat[2][0000−0002−6057−2276], Hajime Nagahara[2][0000−0003−1579−8767], and Ken'ichi Morooka[3][0000−0002−3308−6803]

[1] École Polytechnique, Palaiseau, Paris, France
caioj2906@gmail.com
[2] Osaka University, Osaka, Japan
{sanchayan,sudhakar,nagahara}@ids.osaka-u.ac.jp
[3] Kumamoto University, Kumamoto, Japan
morooka@cs.kumamoto-u.ac.jp

Abstract. Reconstructing 3D volumes from optical microscopic images is useful in important areas such as cellular analysis, cancer research, and drug development. However, existing techniques either require specialized hardware or extensive sample preprocessing. Recently, Yamaguchi *et al.* [20] proposed to solve this problem by just using a single stack of optical microscopic images with different focus settings and reconstructing a voxel-based representation of the observation using the classical iterative optimization method. Inspired by this result, this work aims to explore this method further using new state-of-the-art optimization techniques such as Deep Image Prior (DIP). Our analysis showcases the superiority of this approach over Yamaguchi *et al.* [20] in reconstruction quality, hard metrics, and robustness to noise on the synthetic data. Finally, we also demonstrate the effectiveness of our approach on real data, producing excellent reconstruction quality. Code available at: https://github.com/caiocj1/multifocus-3d-reconstruction.

Keywords: Multi-focus Microscopy · Deep Image Prior · 3D Reconstruction.

1 Introduction

Microscopic images have revolutionized our understanding of the biological processes within various life forms. However, this type of imaging typically ignores vital information encoded in the depth dimension. Avoiding this loss of information is the motivation behind volumetric imaging techniques, which have been a valuable tool to unlock many insights in fields ranging from cancer research and cellular analysis to drug development [4, 3, 17, 19]. The importance, therefore, of developing more accurate and efficient volumetric reconstruction approaches can hardly be overstated.

Various methods have been proposed to capture the volumetric structure of microscopic observations using confocal and electron microscopy techniques [13].

However, the methods based on these techniques often require specialized hardware and extensive preprocessing of samples, which can be expensive and time-consuming. Ideally, we would like to obtain high-fidelity 3D reconstructions using classical imaging techniques such as standard bright-field microscopy, which has become ubiquitous for its relatively simple but effective design.

Although recovering the depth information from a single image is known to be an ill-posed problem [11] when using multiple images, the problem becomes relatively easy to solve and is well-studied; for example, methods focusing on multi-view images [6] and multi-focus images [12, 15]. However, one important drawback of these computer vision-based methods is their general focus on opaque objects. This limits their application to our case, where we need to estimate the volumetric structure of translucent objects (e.g., cells), requiring specialized methods to be developed. Given this context, the question arises:

Can we utilize multiple optical microscopic images to recover the 3D representation of observations?

One of the easiest ways to capture multiple images using an optical microscope is by varying its focus. Recently, Yamaguchi *et al.* [20] first explored this idea by modeling the imaging process of samples by an optical microscope with different focus settings and subsequently reconstructing the 3D volume with the help of an iterative optimization method. Their is compatible with bright-field microscopy and can reconstruct high-quality 3D models from a single, easily obtainable multi-focus stack of images.

Our work revisits Yamaguchi *et al.* [20] and improves it in the following ways: first, we propose a benchmark dataset from the Open-Scivis [10] database by selecting samples with varying complexity of shape and sizes and investigate Yamaguchi *et al.*'s capabilities in reconstructing 3D volumes of samples on this dataset and show that it performs poorly as the complexity of the sample increases. We identify that the classical iterative optimization method is a major reason for this poor performance. Next, to solve these issue, we reformulate the problem of "3D volume reconstruction from multi-focus microscopic images" in the Deep Image Prior (DIP) [16] framework. Our choice of DIP approach to solve this problem is motivated by the following facts: First, the 3D ground-truths of the observed samples are hard to develop. Second, without any ground truths, the DIP approach has proven to be a good candidate for solving inverse problems like ours. Please refer to Figure 1 and Section 3, for our detailed formulation of this problem using DIP. Finally, our analysis of DIP for 3D volume reconstruction shows that the reconstruction quality improves quantitatively and qualitatively, even on complex samples.

2   Related Work

This section discusses various 3D reconstruction methods based on DIP. We also review the existing methods for 3D reconstruction from multi-focus images.

The prospects of DIP have encouraged its use in various 3D reconstruction tasks, especially in medical imaging. For example, Zhou *et al.* [22] used the
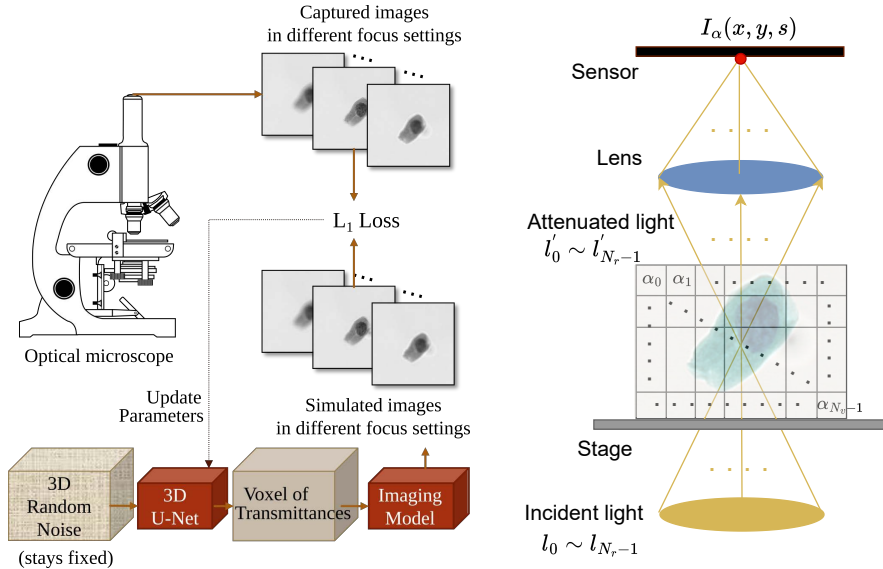
Fig. 1. Illustration of our optimization using DIP (left) and imaging model (right).

DIP framework to effectively address the missing-cone problem in diffraction tomography, improving reconstruction quality. Gong *et al.* [5] introduced the use of the DIP framework for reconstructing 3D PET images. Later, Hashimoto *et al.*[7] built upon the work of Gong *et al.* [5] by introducing an end-to-end block training framework combined with a differentiable forward model. Barbano *et al.*[2] explored various pretraining schemes that lead to significant speed-ups and greatly enhanced training stability on the task of micro-CT reconstruction. In this work, our focus is to use the DIP framework to reconstruct volumetric structures using multi-focus images from an optical microscope.

In the past, reconstruction of 3D structures from multi-focus microscopic images has been attempted in various ways. For example, Abrahamsson *at al.* [1] introduced a mechanism to obtain a stack of multi-focus images instantly (instead of sequentially taking new pictures, which is detrimental to alignment), and reconstructed a 3D model from it by extracting the in-focus regions in each image. Since this leads to high blur in out-of-focus areas, Yoo *et al.*[21] proposed two algorithms that use multiple frames of multi-focus stacks to improve reconstruction quality. Note that the above two works are intended for fluorescence microscopy, and unlike these works, we are interested in general bright-field microscopy which was recently first explored by Yamaguchi *et al.* [20] as discussed in Section 1. We build upon this work and introduce a DIP-based framework to improve it further.
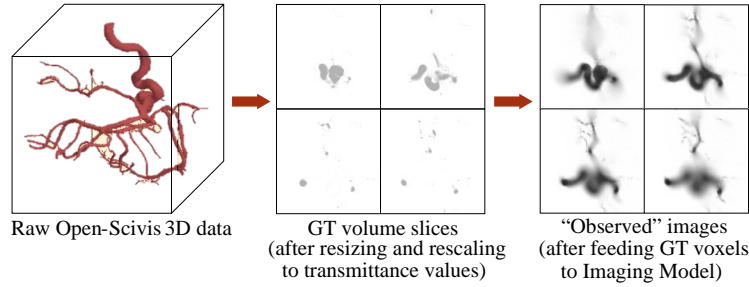
3   Methodology

In this work, we aim to estimate the volumetric structure of a translucent sample via a voxel-based representation utilizing only multi-focus images from an optical microscope. Mathematically, we wish to compute a 3D grid of transmittance values $\alpha_i \in [0, 1]$, where $i = 0, 1, \cdots, N_v - 1$ as shown in Figure 1(right). Here, N_v is the total number of voxels in the 3D grid. We utilize the imaging model described in Yamaguchi *et al.* [20] to synthesize multi-focus images from the 3D grid of transmittance estimates and guide the estimation process by comparing the synthesized images with the ones acquired from a real optical microscope.

Imaging Model. The imaging model works by considering the light as a set of discrete N_r rays that get attenuated as they pass through the 3D grid of N_v voxels, as shown in Figure 1(right). Here, it is assumed that each ray of light gets attenuated solely due to the transmittance values of the voxels and the distance it travels in each voxel in the 3D grid. Mathematically, let l_j and l'_j be the initial and final intensities of the j-th ray of light, respectively. Let d_{ji} be the distance the j-th ray traverses inside a voxel at index i. Note that the j-th ray traverses through multiple voxels at different angles (possibly not all); hence, the d_{ji} for each voxel varies. Also, it gets attenuated as it passes through a voxel according to its transmittance value. Thus, the degree of attenuation of j-th ray depends on which voxels it passes, their transmittance values, and how much distance it travels in each voxel, which can be modeled using Equation 1. Now, assume s represents the focus setting under which an image is taken. After focusing through the 3D grid, the light rays diverge and, through a convergent lens, are refocused at one pixel $I_\alpha(x, y, s)$. Also, an arbitrary pixel can be similarly expressed by shifting the stage along with (x, y, s) coordinates. So, the intensity of a pixel can be computed as the sum of all the final intensities as depicted in Equation 2.

$$l'_j = l_j \prod_i \alpha_i^{d_{ji}}. \qquad (1) \qquad\qquad I_\alpha(x, y, s) = \sum_j l'_j. \qquad (2)$$

Deep Image Prior (DIP) Based Method. Figure 1 (left) illustrates the DIP-based formulation of our problem. Similar to iterative optimization, in our DIP-based approach [16], we minimize the difference between the estimate and the target but without any explicit regularization term. Note that a CNN generates the estimate here, implicitly performing the regularization. Following this idea, we utilize a 3D UNet [14] that takes a random noisy 3D grid as input (which stays fixed during training) and outputs a 3D grid of transmittance estimates, which is then passed through the imaging model to get the simulated images I_α. This is followed by minimizing following L1 loss to optimize the 3D UNet parameters θ: $\mathcal{L}_{DIP}(\theta) = \|I_\alpha - I\|_1$. Here, I is the stack of multi-focus images of the real sample captured by the optical microscope. By updating the parameters, the 3D UNet can reconstruct a 3D grid of transmittance values to produce images similar to the observations.

Raw Open-Scivis 3D data   GT volume slices
(after resizing and rescaling
to transmittance values)   "Observed" images
(after feeding GT voxels
to Imaging Model)

Fig. 2. GT volume generation pipeline and example visualization of a sample.

Pretraining of DIP Network. It is well established that DIP can benefit from the better initialization of 3D UNet in terms of computational speed-up and better overall reconstruction quality [2]. With this in mind, we propose two pretraining strategies for the DIP framework.

Pretr I Pretr I is a reconstruction task where we train the 3D UNet in the DIP framework to fit a ground-truth 3D volume of ellipsoids from a 3D volume of random noise using L2 loss. Using a 3D volume of ellipsoids for reconstruction is motivated by [2], which suggests that ellipsoids constitute good building blocks of complex shapes while being adjusted to fit the volume statistics of objects such as cells. After pretraining, 3D transmittance volume is estimated by initializing the 3D UNet input and its parameters from the above pretraining step.

Pretr II Pretr II is a supervised denoising task. This strategy is a simplified version of the approach used in [2], consisting of a supervised denoising task using the same 3D ellipsoids data as discussed above. We first generate a thousand pairs of noised-denoised 3D volumes of ellipsoids. Next, we train the 3D UNet in the DIP framework to remove noise from the 3D volume of ellipsoids using L2 loss. After pretraining, 3D transmittance volume is estimated by initializing the 3D UNet parameters from the above pretraining step for further training. Details on the construction of the synthetic dataset of 3D volume of ellipsoids are provided in the Supplementary.

In our experiments, whenever one of the two pretraining tasks is not used, we fit the network to a constant value c to stabilize the subsequent training before performing reconstruction on one sample.

Stopping Criterion. When reconstructing from real microscopic images, overfitting to the noise present in the image inevitably occurs unless some stopping criterion is adopted. To solve this issue, we use early-stopping proposed in [18], which tracks the minimal windowed moving variance of the reconstruction sequence and stops the training if it doesn't decrease after certain iterations.

Sample	Iter PSNR	Iter SSIM	DIP (No Pretr) PSNR	DIP (No Pretr) SSIM	DIP + Pretr I PSNR	DIP + Pretr I SSIM	DIP + Pretr II PSNR	DIP + Pretr II SSIM
Aneurism	37.80	0.9863	50.35	0.9992	51.98	0.9994	51.54	0.9993
Backpack	40.02	0.9876	40.55	0.9890	41.07	0.9902	42.00	0.9917
Beechnut	46.54	0.9953	45.23	0.9934	45.72	0.9942	45.63	0.9940
Teapot	44.20	0.9951	45.68	0.9967	46.83	0.9975	46.57	0.9972
Chameleon	41.08	0.9880	43.53	0.9934	43.92	0.9940	44.01	0.9942
Heptane	49.31	0.9981	49.63	0.9985	49.99	0.9986	51.14	0.9988
Engine	38.36	0.9890	45.50	0.9977	44.59	0.9973	45.95	0.9979
Foot	37.90	0.9831	37.47	0.9771	37.82	0.9776	37.33	0.9765
Kingsnake	40.15	0.9839	43.86	0.9918	43.81	0.9922	44.02	0.9922
Lobster	39.25	0.9821	39.67	0.9850	39.46	0.9847	39.75	0.9852
MRI	39.26	0.9942	40.14	0.9852	40.18	0.9857	40.24	0.9856
MRT Angio	45.68	0.9942	44.15	0.9918	44.31	0.9922	44.31	0.9923
Pancreas	43.00	0.9921	44.59	0.9947	45.41	0.9955	44.59	0.9950
Average	41.73	0.9892	43.87	0.9918	44.24	0.9922	**44.39**	**0.9923**

Table 1. Detailed quantitative results from zero-noise 128×128 synthetic images.

4   Experiments

4.1   Experimental Setup

Dataset. Due to the absence of any benchmark dataset for our task, we generate a dataset comprising of 13 synthetic 3D volume ground truths (GTs) using samples from Open-Scivis [10]. The names of the 13 samples are given in Table 1. A visualization of the samples is provided in the Supplementary. Note that the 13 samples are selected for their varying complexity of shape and size. Figure 2 illustrates the pipeline of the synthetic 3D volume GT generation process from the Open-Scivis sample, which is as follows: First, we rescale the samples using trilinear interpolation to smaller sizes. We then normalize the data so that all points in the voxels lie in the range $[0.7, 1.0]$, ensuring that the light reaches the image sensor after passing through the voxels; models with too low transmittance values would produce only black images. Finally, we extract either $50 \times 50 \times 11$ or $128 \times 128 \times 11$ GT volumes so that we can compare how the models perform on more or less complex images. Note that in Figure 2 the z-th volume slice appears in the z-th observed image as the region most in focus. For reproducibility, we also provide the script for the above process in the Supplementary. The synthetic 3D volume GTs are passed through the imaging model to obtain the "observed" images that will be used to reconstruct the desired 3D representation.

Implementation Details. We use Adam optimizer with standard parameters [9] and train on a single NVIDIA V100 32GB GPU for 30 thousand optimization steps. For the iterative optimization method, we use $\mu = 10^{-3}$ as the balancing coefficient of the TV loss, and a constant learning rate $\gamma = 5 \cdot 10^{-3}$. For DIP-based method, a constant learning rate $\gamma = 10^{-3}$ is used. Supplementary Document

shows the architecture of the 3D U-Net in use. Before performing reconstructions with basic DIP (without any pretraining), the initial input noise is fitted to a constant voxel grid of value $c = 0.75$ for 500 steps. We observe that this helps to stabilize the network, as mentioned earlier. Pretr I is performed for 750 optimization steps. Pretr II uses a small dataset of 1000 samples, and training is performed using a batch size of 20 for 5 epochs.

4.2   Results and Analysis

Quantitative Results. In Table 1, we compare the performance of the iterative method (Iter) [20] and our DIP-based method without any pertaining (No Pretr), Pretr I and Pretr II on 128×128. Note that the results correspond to the zero-noise setting. Additionally, the results corresponding to smaller 50×50 images are also provided in Supplementary. We analyze the peak signal-to-noise ratio (PSNR) and structural similarity (SSIM) metrics between reconstructions and ground-truth volumes [8]. We observe that the DIP method widely surpasses the iterative method, with at least 2.14 dB of advantage. We also remark that pretraining DIP improves PSNR by 0.37 dB (Pretr I) and 0.52 dB (Pretr II) over the No Pretr DIP method.

Qualitative Results. In order to have a fuller comprehension of the difference in reconstruction quality between the methods, Figure 3 compares individual slices of the 3D volumes for different samples of the Open-Scivis dataset. Darker pixels indicate voxels with lower transmittance values. Note that the iterative method tends to blur object edges, considerably lowering reconstruction quality.

Robustness Analysis. We compare our method's performance in a more realistic setting by adding centered Gaussian noise with varying variance σ to the observed images. Results are shown in Table 2. All DIP-based settings vastly improve on the previous iterative method: basic DIP has an advantage of 4.21 dB and 3.96 dB for $\sigma = 0.01$ and 0.02, respectively. The benefit from the pretraining is greater when using less noisy images: although for $\sigma = 0.02$, we get advantages of only 0.02 and 0.07 dB using Pretr. I and II, respectively, for $\sigma = 0.01$, we achieve more substantial improvement upon basic DIP, 0.15 and 0.21 dB.

Method	$\sigma = 0.01$		$\sigma = 0.02$	
	PSNR	SSIM	PSNR	SSIM
Iter [20]	35.44	0.9671	34.28	0.9595
DIP	39.65	0.9818	38.24	0.9775
DIP + Pretr. I	39.80	0.9821	38.26	0.9773
DIP + Pretr. II	**39.86**	**0.9824**	**38.31**	**0.9776**

Table 2. Robustness analysis of proposed approach compared to the Iterative method.

	DIP + Early Stopping				
Sample	PSNR	SSIM	Ratio	Time	Itr.
Aneurism	44.38	0.9964	98.95	36	5362
Backpack	34.57	0.9693	98.27	36	4991
Beechnut	42.90	0.9881	99.67	14	2100
Teapot	41.70	0.9921	99.98	42	6279
Chameleon	38.57	0.9802	99.18	15	2319
Heptane	47.45	0.9974	99.52	22	3241
Engine	36.84	0.9888	97.36	19	2861
Foot	34.82	0.9570	99.37	47	6916
Kingsnake	37.13	0.9729	99.23	17	2577
Lobster	35.28	0.9712	99.80	33	4949
MRI	36.20	0.9648	99.23	34	5090
MRT Angio	41.66	0.9856	99.57	8	1271
Pancreas	38.51	0.9730	96.06	24	3566
Average	39.23	0.9798	98.94	27	3963

Table 3. Performance of early-stopping algorithm with DIP, using Gaussian-noised images with $\sigma = 0.01$. The ratio indicates PSNR on the detected stopping point divided by the maximum achieved in the training process. Time is wall-clock time taken in minutes.
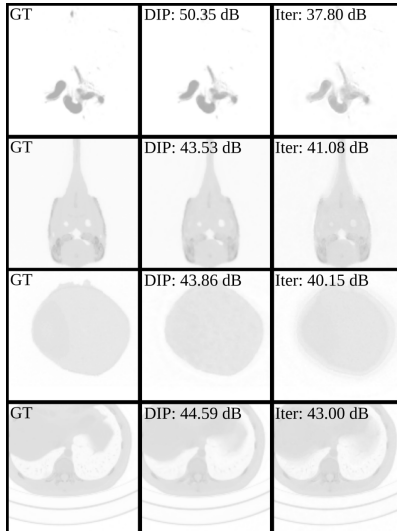
Fig. 3. Qualitative comparison of volume slices between basic DIP model and iterative method for four samples of our evaluation dataset. Samples were chosen to facilitate the visualization of differences.

Early-Stopping Analysis. We simulate a realistic setting and test whether the stopping criterion adopted can propose adequate checkpoints. For this, we again use noisy images with $\sigma = 0.01$ and record the stopping point for each sample. Results are shown in Table 3. With minimal parameter tuning, notice that the early-stopping algorithm can achieve close-to-optimal performance.

Evaluation on Real Data. Finally, we reconstruct 3D volumes from real cell images from an internal dataset to validate our approach using early stopping. The results are shown in Figure 4. Our DIP-based approach can correctly identify the lower transmittance values in different parts of the cell's structure, especially its nucleus. It can also place structures in intermediary depths, representing them in 3D space. Additionally, DIP gives sharp edges, fewer artifacts, and sharper contrast between object and background compared to the iterative method.

5   Conclusion

In this work, we revisit Yamaguchi *et al.*'s [20] method for 3D volume reconstruction from multi-focus optical microscopy images and explore DIP for optimization. We demonstrate that DIP improves the reconstruction quality significantly, both qualitatively and quantitatively. Furthermore, we propose pretraining tasks
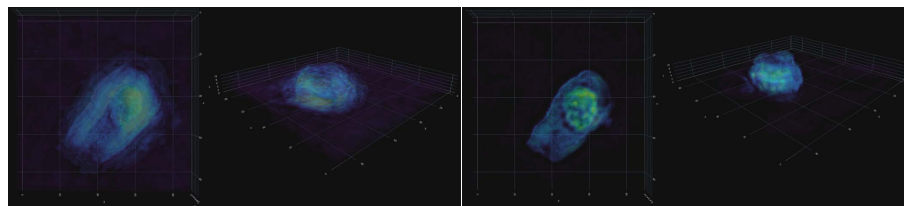
Fig. 4. Reconstruction results on real cell images using Iterative (left) and DIP (right) methods. For each method, a top and side view of the reconstructed 3D cell is presented.

that can circumvent weaknesses inherent to DIP-based approaches and help us achieve even higher reconstruction quality.

Disclosure of Interests. The authors have no competing interests to declare that are relevant to the content of this article.

References

1. Abrahamsson, S., Chen, J., Hajj, B., Stallinga, S., Katsov, A.Y., Wisniewski, J., Mizuguchi, G., Soule, P., Mueller, F., Darzacq, C.D., et al.: Fast multicolor 3D imaging using aberration-corrected multifocus microscopy. Nature Methods **10**(1), 60–63 (2013)
2. Barbano, R., Leuschner, J., Schmidt, M., Denker, A., Hauptmann, A., Maass, P., Jin, B.: An Educated Warm Start for Deep Image Prior-Based Micro CT Reconstruction. IEEE Transactions on Computational Imaging **8**, 1210–1222 (2022)
3. Calì, C., Agus, M., Kare, K., Boges, D.J., Lehväslaiho, H., Hadwiger, M., Magistretti, P.J.: 3d cellular reconstruction of cortical glia and parenchymal morphometric analysis from serial block-face electron microscopy of juvenile rat. Progress in neurobiology **183**, 101696 (2019)
4. Chen, Y., Shen, Q., White, S.L., Gokmen-Polar, Y., Badve, S., Goodman, L.J.: Three-dimensional imaging and quantitative analysis in clarity processed breast cancer tissues. Scientific Reports **9**(1), 5624 (2019)
5. Gong, K., Catana, C., Qi, J., Li, Q.: Pet image reconstruction using deep image prior. IEEE transactions on medical imaging **38**(7), 1655–1665 (2018)
6. Hartley, R., Zisserman, A.: Multiple view geometry in computer vision. Cambridge university press (2003)
7. Hashimoto, F., Onishi, Y., Ote, K., Tashima, H., Yamaya, T.: Fully 3d implementation of the end-to-end deep image prior-based pet image reconstruction using block iterative algorithm. arXiv preprint arXiv:2212.11844 (2022)
8. Horé, A., Ziou, D.: Image quality metrics: Psnr vs. ssim. In: 2010 20th International Conference on Pattern Recognition. pp. 2366–2369 (2010). https://doi.org/10.1109/ICPR.2010.579
9. Kingma, D.P., Ba, J.: Adam: A Method for Stochastic Optimization (2017)

10. Klacansky, P.: Open SciVis Datasets (December 2017), https://klacansky.com/open-scivis-datasets/, `https://klacansky.com/open-scivis-datasets/`

11. Mertan, A., Duff, D.J., Unal, G.: Single image depth estimation: An overview. Digital Signal Processing p. 103441 (2022)

12. Nayar, S.K., Nakagawa, Y.: Shape from focus. IEEE Transactions on Pattern analysis and machine intelligence **16**(8), 824–831 (1994)

13. Peddie, C.J., Collinson, L.M.: Exploring the third dimension: Volume electron microscopy comes of age. Micron **61**, 9–19 (2014). https://doi.org/https://doi.org/10.1016/j.micron.2014.01.009, https://www.sciencedirect.com/science/article/pii/S0968432814000250

14. Ronneberger, O., Fischer, P., Brox, T.: U-net: Convolutional networks for biomedical image segmentation. In: Medical Image Computing and Computer-Assisted Intervention–MICCAI 2015: 18th International Conference, Munich, Germany, October 5-9, 2015, Proceedings, Part III 18. pp. 234–241. Springer (2015)

15. Suwajanakorn, S., Hernandez, C., Seitz, S.M.: Depth from focus with your mobile phone. In: Proceedings of the IEEE Conference on Computer Vision and Pattern Recognition. pp. 3497–3506 (2015)

16. Ulyanov, D., Vedaldi, A., Lempitsky, V.: Deep Image Prior. In: Proceedings of the IEEE Conference on Computer Vision and Pattern Recognition (CVPR) (June 2018)

17. Upla, P., Kim, S.J., Sampathkumar, P., Dutta, K., Cahill, S.M., Chemmama, I.E., Williams, R., Bonanno, J.B., Rice, W.J., Stokes, D.L., Cowburn, D., Almo, S.C., Sali, A., Rout, M.P., Fernandez-Martinez, J.: Molecular architecture of the major membrane ring component of the nuclear pore complex. Structure **25**(3), 434–445 (2017). https://doi.org/https://doi.org/10.1016/j.str.2017.01.006, https://www.sciencedirect.com/science/article/pii/S0969212617300060

18. Wang, H., Li, T., Zhuang, Z., Chen, T., Liang, H., Sun, J.: Early stopping for deep image prior (2022)

19. Wenzel, C., Riefke, B., Gründemann, S., Krebs, A., Christian, S., Prinz, F., Osterland, M., Golfier, S., Räse, S., Ansari, N., Esner, M., Bickle, M., Pampaloni, F., Mattheyer, C., Stelzer, E.H., Parczyk, K., Prechtl, S., Steigemann, P.: 3d high-content screening for the identification of compounds that target cells in dormant tumor spheroid regions. Experimental Cell Research **323**(1), 131–143 (2014). https://doi.org/https://doi.org/10.1016/j.yexcr.2014.01.017, https://www.sciencedirect.com/science/article/pii/S0014482714000263

20. Yamaguchi, T., Nagahara, H., Morooka, K., Nakashima, Y., Uranishi, Y., Miyauchi, S., Kurazume, R.: 3D Image Reconstruction from Multi-focus Microscopic Images. In: Dabrowski, J.J., Rahman, A., Paul, M. (eds.) Image and Video Technology. pp. 73–85. Springer International Publishing, Cham (2020)

21. Yoo, S., Ruiz, P., Huang, X., He, K., Ferrier, N.J., Hereld, M., Selewa, A., Daddysman, M., Scherer, N., Cossairt, O., Katsaggelos, A.K.: 3D Image Reconstruction from Multi-Focus Microscope: Axial Super-Resolution and Multiple-Frame Processing. In: 2018 IEEE International Conference on Acoustics, Speech and Signal Processing (ICASSP). pp. 1453–1457 (2018). https://doi.org/10.1109/ICASSP.2018.8462234

22. Zhou, K.C., Horstmeyer, R.: Diffraction tomography with a deep image prior. Optics express **28**(9), 12872–12896 (2020)